IEEE Access
Multidisciplinary | Rapid Review | Open Access Journal

Received 21 June 2024, accepted 27 July 2024, date of publication 2 August 2024, date of current version 13 August 2024.

Digital Object Identifier 10.1109/ACCESS.2024.3437428

RESEARCH ARTICLE

Sensorless Control of Permanent Magnet Synchronous Motors Based on Novel Position Angle Extraction With SMO

CHEN ZHANG, XIAO TANG, KUN XING, AND HENGRUI ZHOU
Faculty of Automation, Huaiyin Institute of Technology, Huaian, Jiangsu 223003, China
Corresponding author: Chen Zhang (12080010@hyit.edu.cn)

ABSTRACT This paper presents an improved sensorless controller scheme for a robust permanent magnet synchronous motor. Firstly, a sliding mode observer based on a variable rate approach rate is designed to observe the back electromotive force, enhance the robustness of the back electromotive force acquisition process, and reduce the system buffeting. Secondly, the concept of finite control set model predictive control is introduced, and the position angles are divided into small angles to form finite control sets. Then the position Angle of the finite control set is entered into the sliding mode observer to calculate the back electromotive force. At the same time, the optimal position angle is obtained based on the cost function of the back electromotive force. In order to reduce the number of iterations, the dichotomy is adopted to reduce unnecessary calculations. The proposed finite position-set phase-locked loop (PLL) avoids the PI controller in the traditional PLL and further improves the robustness of the system. Finally, the effectiveness of the proposed scheme is verified by relevant experiments.

INDEX TERMS Sensorless control, finite position set, phase locked loop, sliding mode observer.

I. INTRODUCTION

In recent years, with the excessive consumption of non-renewable resources, more and more scholars and engineers have focused on the new energy industry. With the rise of the new energy industry, all kinds of drive motors have been widely used in industrial fields, such as the electrical vehicles, marine, and aerospace industries [1], [2], [3], [4], [5]. Among them, permanent magnet synchronous motor (PMSM) has attracted much attention due to its advantages such as high-power density, high efficiency, and large torque-to-current ratio [6], [7], [8], [9]. Correspondingly, more and more high-performance control schemes such as magnetic field-oriented control, direct torque control, sliding mode control, and model predictive control are studied to improve the control [10], [11], [12], [13], [14], [15] performance of PMSM. The effective implementation of such schemes depends on accurate rotor position and velocity information. However, the installation of mechanical sensors increases the complexity and cost of the system and also reduces the reliability of the system. Therefore, the sensorless control strategy has received more and more attention [16], [17], [18], [19], [20].

Sensorless control can be roughly divided into salient pole type and fundamental wave type according to the categories of extracted information. The former utilizes the salient pole effect of PMSM to extract the control quantity through external signal injection [21], [22], [23]. The latter depends on its own change in the operation of the motor, such as back electromotive force, stator current, voltage, etc., through these parameters to calculate the extraction of position information [24], [25], [26]. High-frequency signal injection methods mainly include the high-frequency voltage injection method [27] and the high-frequency current injection method [28]. These schemes mainly use the salient pole of the motor to estimate the rotor angle and solve the problem of parameter estimation at the low speed or zero speed of the motor. The high frequency voltage injection

The associate editor coordinating the review of this manuscript and approving it for publication was Feifei Bu.

method can accurately estimate the rotor position of the internal PMSM at low speeds, and the high frequency current injection method can use devices with low forward voltage drop for high frequency applications, reducing the need for carrier life technology [29].

The fundamental mode sensorless control method has two representatives, that is, the back electromotive force (EMF) method and the model reference adaptive system (MRAS). The main idea of MRAS is to take the mathematical model of parameter determination as the control reference model and obtain a dynamic adjusting feedback control law so that the closed-loop control performance of the system can be consistent with the performance of the reference model [30]. The back EMF method is mainly aimed at the surface-mounted PMSM, which needs to construct an observer to extract the back EMF and obtain the position angle and speed value from the back EMF by using the trigonometric function. Commonly used observers include sliding mode observer (SMO) [31], Kalman filter observer, and disturbance observer [32].

In [31], an enhanced s SMO with current compensation is proposed. The fuzzy logic controller is used to realize the shape coefficient adaptive SMO based on the hyperbolic tangent switching function. In [33], a synovial observer method with delay suppression is proposed. Not only the hyperbolic function of the appropriate boundary layer is used to eliminate chattering, but also a current compensation method with a dual sampling strategy is proposed. In addition, [34] uses the minimum order observer to estimate the extended reaction electromotive force to obtain the speed information and estimate the position error.

Extracting position information based on back EMF has become a mainstream method in the sensorless field. To reduce the buffeting caused by the inverse tangent function, a phase-locked loop (PLL) is widely used. A sensorless control method based on robust observer and non-orthogonal PLL is proposed in [35]. This method takes robustness into account to ensure that the motor can still operate effectively in the case of phase loss and short circuit faults. A rotor position estimation method based on PLL and third-order steady-state linear Kalman filter is proposed in [36]. However, the PI controller with a fixed gain is generally used to estimate the rotor position in the above PLL, and the parameter uncertainty, unmodeled dynamics, and external interference during system operation will make it difficult for the PI controller to meet the output performance [37], [38], [39], [40]. A finite position set PLL is proposed in [39]. The back EMF is calculated by discrete position angle and the optimal position angle and rotation speed are obtained by substituting the cost function. This scheme avoids the use of a PI controller. On this basis, a dichotomy-based position angle iteration algorithm is proposed in [41] to reduce the computational burden of non-sensing schemes. However, the calculation of the back EMF in the above scheme depends on the parameters of the motor and lacks robustness.

Therefore, this paper proposes a method to combine improved SMO with enhanced FPS-PLL. In order to solve the chattering problem inherent in traditional SMO, the super torsion function is used instead of the symbolic function to suppress the chattering problem. At the same time, the motor parameter adaptive SMO is designed to enhance the robustness of the system and improve the accuracy of rotor position estimation. The traditional PLL was replaced by FPS-PLL to further improve robustness, using dichotomies to speed up computation.

The rest of this paper consists of five parts. The second part gives the mathematical modeling of the three-phase permanent magnet synchronous motor. Then, in the third section, the traditional PI-based PLL structure and the finite position set PLL structure are proposed. In the fourth part, an improved sliding mode observer and a finite position-set phase-locked loop based on dichotomy are presented. Finally, the fifth and sixth parts are experimental verification and conclusion respectively.

II. DRIVE SYSTEM MODEL OF THREE-PHASE PMSM

Three-phase PMSM is the research object of this paper. Because the permanent magnet used in PMSM is surface-mounted, the d-axis and q-axis inductance are equal ($L_d = L_q = L_s$).

The voltage equation of PMSM in the d-q rotating coordinate system can be expressed as follows:

$$\boldsymbol{u} = \boldsymbol{A}\boldsymbol{i} + \boldsymbol{B}\frac{d}{dt}\boldsymbol{i} + \boldsymbol{C} \tag{1}$$

where

$$\boldsymbol{u} = \begin{bmatrix} u_d \\ u_q \end{bmatrix}; \boldsymbol{i} = \begin{bmatrix} i_d \\ i_q \end{bmatrix}; \boldsymbol{A} = \begin{bmatrix} R_s & -\omega_e L_s \\ \omega_e L_s & R_s \end{bmatrix};$$
$$\boldsymbol{B} = \begin{bmatrix} L_s & 0 \\ 0 & L_s \end{bmatrix}; \boldsymbol{C} = \begin{bmatrix} 0 \\ \omega_e \psi_f \end{bmatrix}$$

$\boldsymbol{u}$ and $\boldsymbol{i}$ represent the voltage and current respectively, and ω_e is the electric angular velocity. R_s and ψ_f represent stator resistance and flux linkage.

The electromagnetic torque equation of the surface-mounted permanent magnet synchronous motor (SPMSM) is given by:

$$T_e = \frac{3}{2} P_n i_q \psi_f \tag{2}$$

where P_n represents the number of pole pairs.

The mechanical equation of SPMSM is expressed as follows:

$$J\frac{d\omega_m}{dt} = T_e - T_L - B\omega_m \tag{3}$$

where J, ω_m, B, and T_L represent the moment of inertia, mechanical angular velocity, friction coefficient, and load of the motor, respectively.

III. TRADITIONAL PLL AND FINITE POSITION SET PLL

The matrix $\boldsymbol{C}$ in (1) can simultaneously be expressed as the back EMF of the PMSM. Therefore, according to [41], it is necessary to obtain the discrete model of PMSM before obtaining the back EMF as follows:

$$\boldsymbol{u}(k) = \boldsymbol{A}_1\boldsymbol{i}(k) + \boldsymbol{B}_1\boldsymbol{i}(k+1) + \boldsymbol{E}(k) \tag{4}$$

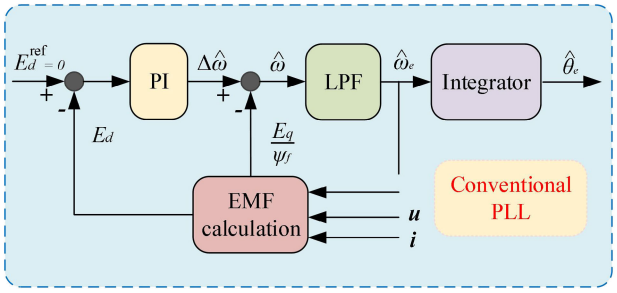

FIGURE 1. Conventional PLL structure.

where

$$\boldsymbol{A}_1 = \begin{bmatrix} R_s - \frac{L_s}{T_s} & -\omega_e(k)L_s \\ \omega_e(k)L_s & R_s - \frac{L_s}{T_s} \end{bmatrix}, \boldsymbol{B}_1 = \begin{bmatrix} \frac{L_s}{T_s} & 0 \\ 0 & \frac{L_s}{T_s} \end{bmatrix}, \boldsymbol{E} = \boldsymbol{C}$$

where k and $k+1$ represent the value of the current time and the next time respectively, and T_s represents the sampling period. The back EMF $\boldsymbol{E} = [E_d, E_q]^{\mathrm{T}}$ can be derived from (4):

$$\boldsymbol{E}(k) = \boldsymbol{u}(k) - \boldsymbol{A}_1\boldsymbol{i}(k) - \boldsymbol{B}_1\boldsymbol{i}(k+1) \tag{5}$$

After obtaining the back electromotive force, the structure of conventional PLL extraction speed and position angle is shown in Fig. 1.

The difference between the d-axis calculated component of the back electromotive force and the reference value generates the change of speed through PI, and the estimated speed is obtained through feedforward compensation and low pass filter (LPF), and the position angle is further integrated.

On this basis, a finite position set phase-locked loop (FPS-PLL) is proposed in [38]. This scheme avoids the use of PI controllers and improves the reliability and robustness of the system under complex conditions. The idea of a finite location set comes from the finite control set model predictive control (FCS-MPC), and its specific principle is as follows:

FCS-MPC has a fixed number of voltage vectors because it uses the discrete nature of the inverter. These voltage vectors are substituted into the prediction model to obtain the predicted value of the controlled variable. By substituting the predicted value into the cost function, the optimal voltage vector is calculated online and output to the inverter. Finally, repeat the above steps. Taking finite control set model predictive current control as an example, the whole control process includes three parts: predictive model, cost function, and rolling optimization, and its specific block diagram is shown in Fig. 2.

According to the principle of FCS-MPC, a finite set of positions is formed by dividing the unknown position angles into small angles. Its control block diagram is shown in Fig. 3.

The discretization of the finite position angle uses two nesting, and its discretization equation is as follows

$$\begin{cases} \theta_{i,j}(k) = \theta_{ini,i}(k) + (j-4)\Delta\theta_i(k) \\ \Delta\theta_i(k) = 2^{-i-2} \cdot \pi \end{cases} \tag{6}$$

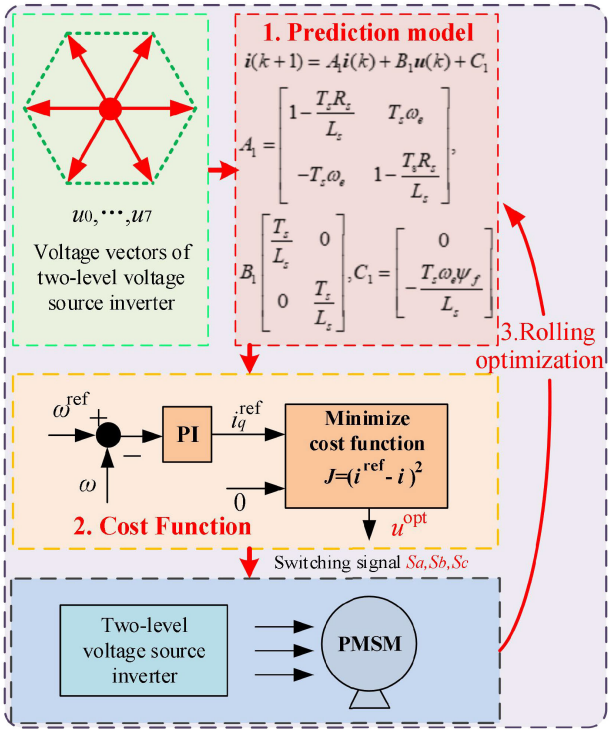

FIGURE 2. Schematic diagram of FCS-MPC.

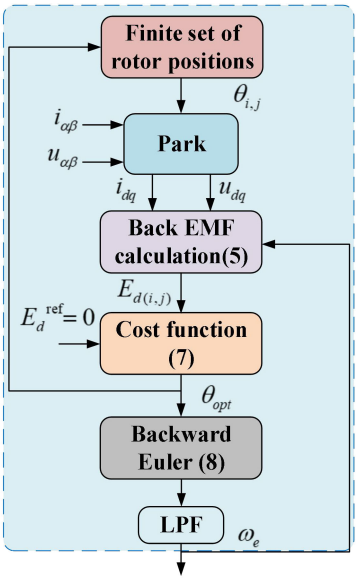

FIGURE 3. The structure of a phase-locked loop with finite position sets.

The cost function of FPS-PLL design is used to minimize the reference back electromotive force and to predict the back electromotive force, so the control problem can be summarized as follows

$$J = E_d^{\mathrm{ref}} - E_{d(i,j)} \tag{7}$$

As shown in Fig. 4, when the optimal value obtained by the first iteration (i = 0, j = 0∼7) is $\pi/2$, the discrete position

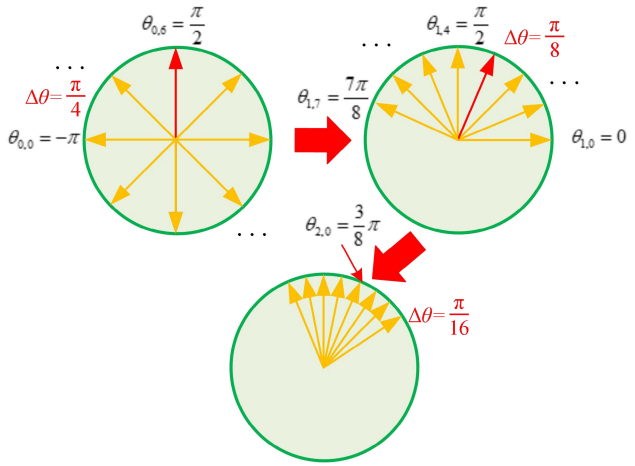

FIGURE 4. Angular discretization rules for finite position sets.

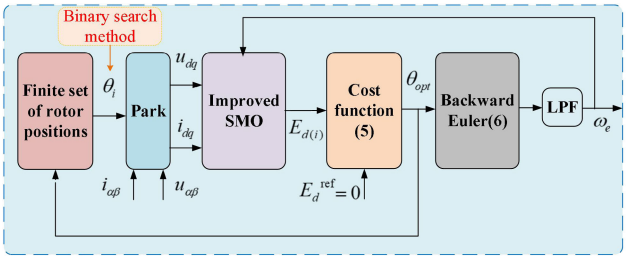

FIGURE 5. Improved sensorless control strategy.

angle of the second iteration (i = 1, j = 0∼7) is shown in $\pi/2+(j-4)^*\pi/2$, And iterate until the end of 64 iterations.

After obtaining the optimal position angle θ_{opt}, the rotational speed can be obtained by the Euler discrete method:

$$\omega_e(k)=\frac{\theta_{opt}(k)-\theta_{opt}(k-1)}{T_s} \tag{8}$$

In addition, the stability of FPS-PLL in terms of tracking error was demonstrated in [42].

IV. THE PROPOSED SENSORLESS CONTROL SCHEME

To improve the robustness of back electromotive force, this chapter designs an improved sliding mode observer (SMO) to estimate back electromotive force instead of the traditional calculation scheme. In addition, in order to reduce the computational burden of PLL with finite position sets, the binary method is used to replace the traditional FPS-PLL search process. The control block diagram of the overall scheme is shown in Fig. 5.

A. IMPROVED SLIDING MODE OBSERVER

The expression of the back electromotive force in the two-phase rest coordinate system is as follows:

$$\begin{bmatrix}E_\alpha\\E_\beta\end{bmatrix}=\omega_e\psi_f\begin{bmatrix}-\sin\theta_e\\\cos\theta_e\end{bmatrix} \tag{9}$$

As shown in (9), the rotor position information is only contained in the extended electromotive force component. Therefore, once the extended counter-potential component can be estimated, the rotor position information can be obtained directly.

Therefore, in order to obtain information on the rotor position and speed of the motor, a sliding mode observer is constructed based on the voltage equation as follows:

$$\frac{d}{dt}\begin{bmatrix}\tilde{i}_\alpha\\\tilde{i}_\beta\end{bmatrix}=-\frac{R_s}{L_s}\begin{bmatrix}\tilde{i}_\alpha\\\tilde{i}_\beta\end{bmatrix}+\frac{1}{L_s}\begin{bmatrix}\tilde{E}_\alpha\\\tilde{E}_\beta\end{bmatrix} \tag{10}$$

where '∼' represents the error between the observed value obtained by the observer and the actual value.

To obtain the extended reaction electromotive force, the current error value is taken as the sliding mode surface in SMO, and the traditional sliding mode control rate is expressed as:

$$\hat{\boldsymbol{E}}=k_s\mathrm{sgn}\left(\hat{\boldsymbol{i}}_s-\boldsymbol{i}_s\right) \tag{11}$$

where k_s is the gain coefficient. When $s=\hat{\boldsymbol{i}}_s-\boldsymbol{i}_s=0$, the error between the estimated velocity and the actual velocity is small enough, then the estimated extended electromotive force is:

$$\hat{\boldsymbol{E}}=\boldsymbol{E} \tag{12}$$

To satisfy the stability of the SMO, k_s has to satisfy the following conditions:

$$k_s\geq\max(\boldsymbol{E}\mathrm{sgn}(\boldsymbol{s})-R_s|\boldsymbol{s}|) \tag{13}$$

However, due to the serious drawbacks of the conventional isokinetic convergence rate, the gain coefficient is usually modulated to be larger in order to reach the sliding mode surface quickly. However, this also leads to severe jitter as the state volume approaches the sliding mode plane. This leads to a large amount of high-frequency jitter in the estimated variables, and further errors in the extraction of the position angle by the inverse tangent function, which, despite the design of the filter, also results in phase errors and makes angular compensation cumbersome. Therefore, the SMO with a new approach rate is developed and the angle extraction method is optimized for the above problems.

First, the hyperbolic function is used as the switching function. Its upper and lower bounds are the same, but tan$K$(s) further reduces the jitter of the SMO by smoothing the curve control instead of the discontinuous step function. In addition, the hyperbolic function is continuous and the function has no time lag properties, the expression of which is shown in (14).

$$g(s)=\tan K(s)=\frac{\exp(s)-\exp(-s)}{\exp(s)+\exp(-s)} \tag{14}$$

In addition, in order to ensure that the system has a fast convergence rate when moving away from the slip form surface and at the same time reduce the high-frequency jitter effect when reaching the slip form surface. Therefore, a new convergence rate is reconstructed as shown in (15). This

replaces sgn(s) with an isokinetic convergence rate and has a variable speed effect.

$$\frac{ds}{dt} = h(u_1, s)g(s) + f(s) \tag{15}$$

$$f(s) = -\delta s \tag{16}$$

$$h(u_1, s) = -\frac{k_s |u_1|}{a(|u_1| + \lambda e^{-\varepsilon|s|}) + |u_1| e^{-\varepsilon|s|}} \tag{17}$$

where $\lambda > 0$, $\delta > 0$, $\varepsilon > 0$, $0 < a < 1$, u_1 is the system state quantity. As known from (16) and (17), $h(u_1, s)$ varies with the system state volume and the sliding mode switching surface s.

From the above original convergence rates, it can be seen that in case the system state is far from the sliding mode switching surface, (when the sliding mode switching function $|s|$ converges to ∞).

$$\lim_{s\to\infty} a(|u_1| + \lambda e^{-\varepsilon|s|}) + |u_1| e^{-\varepsilon|s|} = a|u_1| \tag{18}$$

As a result, $h(u_1, s)$ converges to the constant k_s/a ($k_s/a > k_s$), while $f(s)$ converges to ∞, further increasing the system convergence rate. On the other hand, when the system state is close to the slip form surface (when $|s|$ tends to 0), so $f(s) \to 0$.

$$\lim_{s\to 0}[h(u_1, s) \cdot g(s) + f(s)] = \frac{k_s |u_1|}{(a+1)|u_1| + \lambda} \tag{19}$$

that the system state will gradually decrease to 0 as it approaches the switching plane s, thus achieving the purpose of dither suppression.

B. STABILITY ANALYSIS

In this section, the Lyapunov function is usually chosen to verify the stability of the novel convergence rate.

$$\dot{V} = s\dot{s} = -\frac{k_s |u_1| \cdot s}{a(|u_1| + \lambda e^{-\varepsilon|s|}) + |u_1| e^{-\varepsilon|s|}} \times \tan K(s) - \delta s^2 \le 0 \tag{20}$$

There are three scenarios that should be discussed.

Case 1: when $s > 0$, $a(|u_1| + \lambda e^{-\varepsilon|s|}) + |u_1| e^{-\varepsilon|s|} > 0$, $\tan K(s) > 0$, $k_s |u_1| > 0$, $-\delta s^2 < 0$, So $\dot{V} < 0$, it meets the conditions.

Case 2: when $s < 0$, $\frac{k_s|u_1|\cdot s}{a(|u_1|+\lambda e^{-\varepsilon|s|})+|u_1|e^{-\varepsilon|s|}} > 0$, $\tan K(s) < 0$, $-\delta s^2 < 0$, So $\dot{V} < 0$, it also meets the (19).

Case 3: when $s = 0$, $\frac{k_s|u_1|\cdot s}{a(|u_1|+\lambda e^{-\varepsilon|s|})+|u_1|e^{-\varepsilon|s|}} = 0$, $\tan K(s) = 0$, $-\delta s^2 < 0$, So $\dot{V} < 0$, this situation satisfies $\dot{V} \le 0$.

According to the above three cases, the proposed convergence rate satisfies the arrival condition of the sliding mode and can guarantee that the system motion trajectory reaches the sliding mode switching surface in a finite time.

C. FPS-PLL BASED ON DICHOTOMY

As can be seen from Fig. 4, some position angles in the second iteration overlap with those in the first iteration, which undoubtedly increases the unnecessary calculation burden.

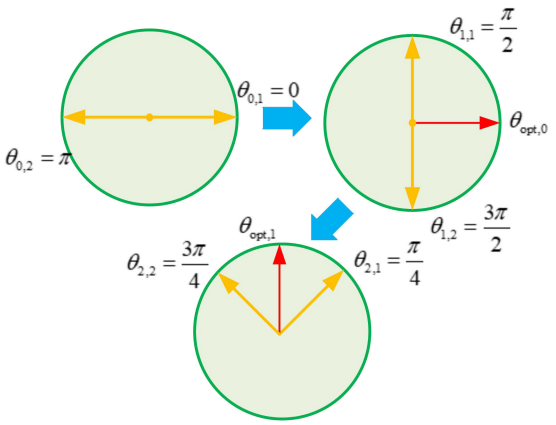

FIGURE 6. At the same time, the system state will gradually converge to 0 under the action of sliding mode control, which indicates Position discretization scheme based on dichotomy.

Therefore, the dichotom-based position discrete calculation scheme as shown in Fig. 6 is adopted.

The steps of the proposed scheme are as follows:

Step 1: Firstly, the discrete angle is set to $\theta_{j,i}(i = 1,2$ and $j = 0\sim7)$, there are 8 iterations in total, and the optimal position angle obtained in each iteration is $\theta_{opt,j}$,

Step 2: Set the initial angles $\theta_{0,1}$ and $\theta_{0,2}$ to 0 and π respectively to obtain the back electromotive force, and then substitute the cost function to calculate its optimal value $\theta_{opt,0}$,

Step 3: Set $\Delta\theta = \pi * 2^{-j}$, apply the $\theta_{opt,0}$ obtained in step 2 and the $\theta_{1,1}$ and $\theta_{1,2}$ discretized from $\Delta\theta$ to the back electromotive force, and then enter the cost function to calculate the optimal value $\theta_{opt,1}$.

Step 4: Repeat steps 2 and 3 until $j = 7$ to output the final optimal position angle.

The main advantage of FPS-PLL is to avoid the PI controller in the case of searching for the optimal rotor position angle. The angle fluctuation obtained by the optimal value depends on the accuracy of the dichotomy. The precision of PLL is inversely proportional to the number of iterations. Finally, the optimal rotor position angle selected by iteration can maintain the accuracy of $\pi \times 2^{-8} = 0.012$ rad. In order to improve the readability of the proposed scheme, Fig. 7 provides a flow chart of the key algorithms.

V. EXPERIMENTAL RESULT

Fig. 8 shows the construction of the experimental device, and the relevant SPMSM parameters are shown in Table 1. In order to verify the effectiveness of the proposed scheme under sensorless operation, the performance of position tracking and speed tracking is verified by experiments. The real-time digital controller RTU-BOX201 provided by rtunit was used in the experiment, and the control period was set to 100μs. The parameters of the sliding mode observer are set as $k_s = 200$, $\lambda = 10$, $\delta = 10$, $\varepsilon = 5$ and $a = 0.5$.

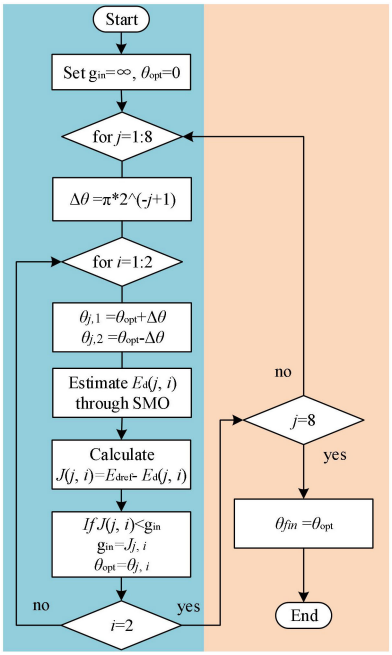

FIGURE 7. The flow chart of the implementation of the proposed SMO+FPS-PLL.

FIGURE 8. The experiment platform.

TABLE 1. SPMSM system parameters.

Symbol	Parameters	Values
L_s	Inductance	6.6 mH
R_s	Resistance	1.6 Ω
Pn	Number of pole pairs	4
N^{ref}	Rated speed	2500 rpm
P	Rated power	3.8 kW
T_e	Rated torque	15 Nm
J	Inertia	0.00277 kg.m^2

In this section, in order to verify the effectiveness of the proposed method, it is compared with traditional PLL based on a PI controller.

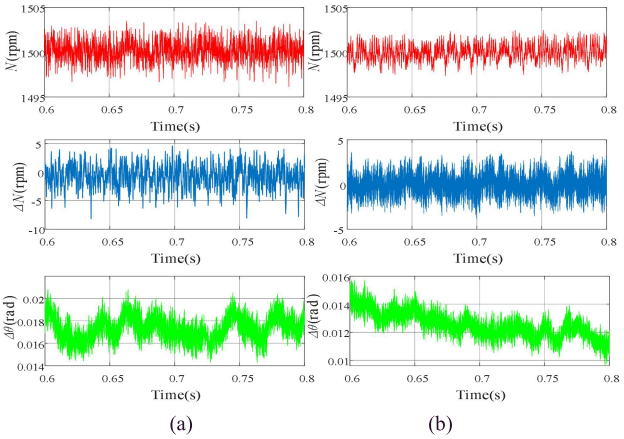

FIGURE 9. Steady-state performance experiment in fixed speed and toque. (a) Conventional PLL (b) Proposed Method.

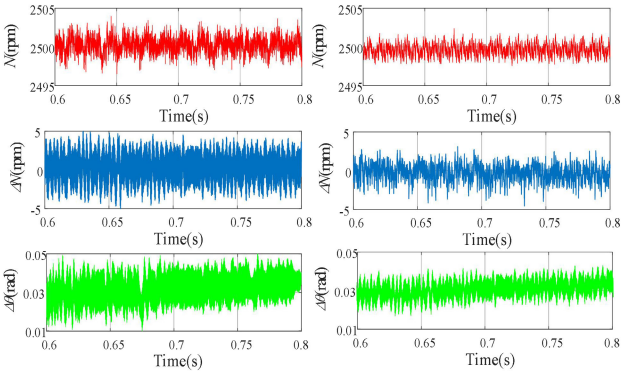

FIGURE 10. Steady-state performance experiment in 2500rpm. (a) Conventional PLL (b) Proposed Method.

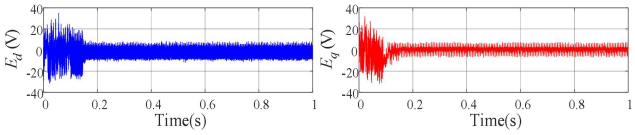

FIGURE 11. Variation diagram of d-q axis back electromotive force waveform.

Fig. 9 shows the motor speed, speed error, and rotor position angle error at 1500rpm and 10Nm. It can be observed that the two methods have good performance in the stability experiment, the proposed scheme has less velocity fluctuation and angle error, and the estimated position angle is more accurate. Fig. 10 shows the motor speed, speed error and rotor position angle error at rated speed, which is consistent with the performance shown in Fig. 9.

The back electromotive force waveform of the proposed scheme fluctuates greatly at zero speed and low speed, which is not conducive to the observer's estimation of speed. Fig. 11 shows the back electromotive force waveform of d-q axis with no load at rated speed.

Under the conditions of changing speed, it can be clearly seen from Fig. 12 that the overshoot of the traditional method

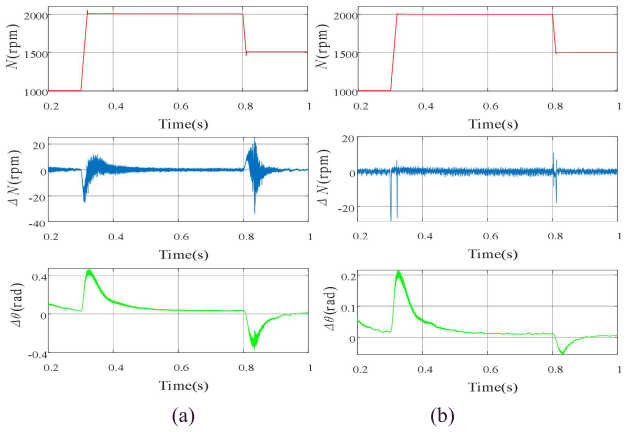

FIGURE 12. The speed suddenly changes from 1000 rpm to 2000 rpm and then decreases to 1500 rpm, and the torque is fixed at 10 Nm. (a) Conventional PLL (b) Proposed Method.

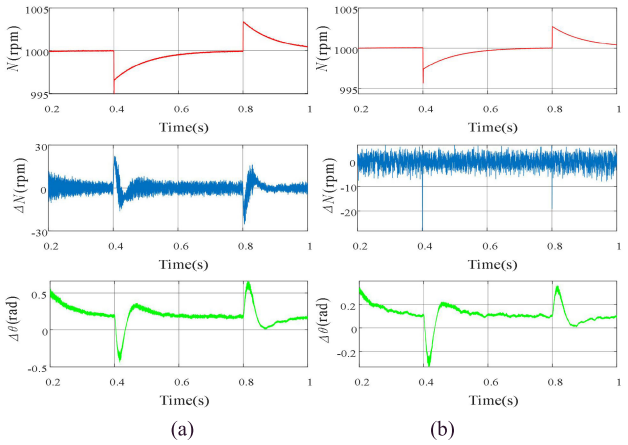

FIGURE 13. Torque mutation test. The motor started with load and accelerated to 1000rpm. The load increased from 5Nm to 10Nm and then decreased to 5Nm. (a) Conventional PLL (b) Proposed Method.

is larger. The main reason is that PLL with fixed gain PI cannot converge effectively when the operating conditions change suddenly. The speed error of the proposed method is about 27rpm, while the maximum error of the traditional method is 36rpm and the maximum position error is 0.49 rad. When the load changes, as shown in Fig. 13, the position angle error of the traditional method is 0.52rad, while the maximum error of the proposed scheme is 0.22rad. It can be observed that the dynamic performance of the proposed method is as good as the steady-state performance.

In order to verify the robustness of the proposed method, the parameter mismatch is simulated by changing the motor parameters in the controller, because the motor cannot change the parameter size at any time according to the setting during operation. The whole experiment was tested when the speed was stable at 1000rpm. It can be clearly seen from Fig. 14 that when the inductance ($0.5L_s$) is changed, the speed of the traditional method has serious buffeting, and the max speed error is 18 rpm. However, the proposed methods are almost

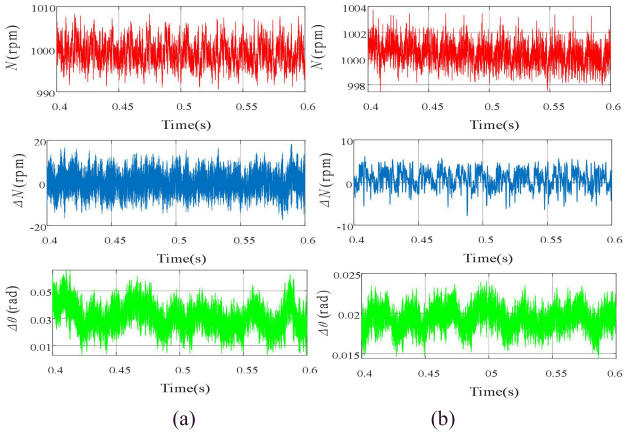

FIGURE 14. Experimental performance under 50%L_s (a) Conventional PLL (b) Proposed Method.

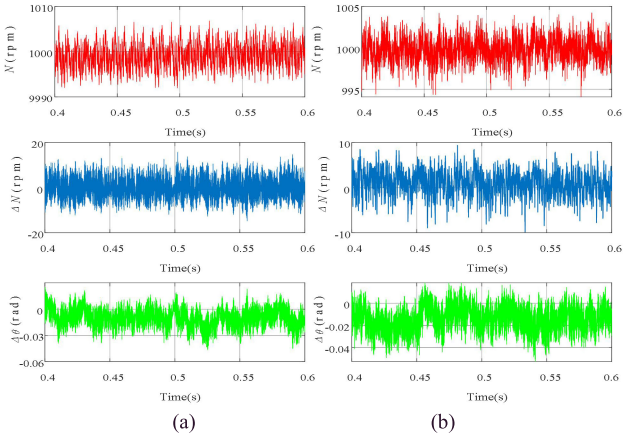

FIGURE 15. Experimental performance under 0.5R_s (a) Conventional PLL (b) Proposed Method.

TABLE 2. Comparison of calculation time.

Methods	FPS-PLL in [38]	The proposed scheme
Calculation time	63μs	46μs

unaffected. The proposed scheme can converge effectively and its position angle error is about 0.02rad.

In order to fully demonstrate the robustness of the proposed method. As shown in Fig. 15, the position estimation performance of the two schemes is verified when the resistance meets $0.5R_s$, and the velocity error and position angle estimation error of the proposed method is smaller than that of the traditional method.

In summary, the proposed scheme has good position estimation ability in both steady-state and dynamic tests, and can effectively reduce parameter sensitivity.

To demonstrate the advantages of the proposed dichotomy, the authors compare the computation time of the proposed scheme with that of FPS-PLL in [38]. As shown in Table 2,

the execution cycle of the proposed scheme is 46μs, which is smaller than 63μs of the scheme adopted in [38]. Therefore, the proposed scheme has a smaller computational burden.

VI. CONCLUSION

In this paper, a sensorless control scheme of a three-phase permanent magnet synchronous motor based on a finite position set phase-locked loop is proposed. Firstly, the exponential approximation rate of the velocity is designed, and the hyperbolic inverse tangent function is used instead of the sign function to solve the buffering problem of the approximation rate of the traditional sliding mode observer. The sliding mode observer is used to estimate the back electromotive force, which improves the robustness of the system and is beneficial to the operation of the motor in complex environment. Then, the position angle is discretized based on dichotomy, and the optimal position angle is found by iterative search. With the increase in the number of iterations, the estimation accuracy of the algorithm increases geometrically. Finally, the experimental results show that the proposed method has smaller rotor speed estimation error, higher position estimation accuracy and better system robustness, and the dichotomy method can effectively reduce the calculation burden of FPS-PLL. However, sensorless schemes based on back electromotive force have large back potential fluctuations at zero velocity and low temperature, which is not conducive to position estimation. In the future, the authors will consider non-sensing schemes in the full speed range and explore effective switching methods from low to high speed.

REFERENCES

[1] C.-H. Seok, S.-Y. Yoon, H.-S. Choi, H.-Y. Lee, and J. Seo, "Analysis and modeling of axial leakage for spoke-type hybrid permanent magnet machines," *IEEE Access*, vol. 11, pp. 6385–6393, 2023.

[2] Z. Shi, "Design optimization of a spoke-type axial-flux PM machine for in-wheel drive operation," *IEEE Trans. Transport. Electrific.*, vol. 10, no. 2, pp. 3770–3781, Jun. 2024, doi: 10.1109/TTE.2023.3310738.

[3] E. Trancho, E. Ibarra, A. Arias, I. Kortabarria, P. Prieto, I. M. de Alegría, J. Andreu, and I. López, "Sensorless control strategy for light-duty EVs and efficiency loss evaluation of high frequency injection under standardized urban driving cycles," *Appl. Energy*, vol. 224, pp. 647–658, Aug. 2018.

[4] X. Sun, N. Xu, M. Yao, F. Cai, and M. Wu, "Efficient feedback linearization control for an IPMSM of EVs based on improved firefly algorithm," *ISA Trans.*, vol. 134, pp. 431–441, Mar. 2023.

[5] W. Xu, H. Chen, J. Wang, and H. Zhao, "Velocity optimization for braking energy management of in-wheel motor electric vehicles," *IEEE Access*, vol. 7, pp. 66410–66422, 2019.

[6] X. Sun, Z. Shi, Y. Cai, G. Lei, Y. Guo, and J. Zhu, "Driving-cycle-oriented design optimization of a permanent magnet hub motor drive system for a four-wheel-drive electric vehicle," *IEEE Trans. Transport. Electrific.*, vol. 6, no. 3, pp. 1115–1125, Sep. 2020.

[7] M. Suphama, P. Seangwong, N. Fernando, J. Jongudomkarn, A. Siritaratiwat, and P. Khunkitti, "A novel asymmetric hybrid-layer del-shaped rotor interior permanent magnet motor for electric vehicles," *IEEE Access*, vol. 12, pp. 2793–2802, 2024.

[8] X. Sun, Z. Su, G. Lei, and M. Yao, "Robust predictive cascaded speed and current control for PMSM drives considering parameter variations," *IEEE Trans. Ind. Electron.*, vol. 71, no. 9, pp. 10235–10245, Sep. 2024, doi: 10.1109/TIE.2023.3337498.

[9] Z. Shi, X. Sun, Y. Cai, Z. Yang, G. Lei, Y. Guo, and J. Zhu, "Torque analysis and dynamic performance improvement of a PMSM for EVs by skew angle optimization," *IEEE Trans. Appl. Supercond.*, vol. 29, no. 2, pp. 1–5, Mar. 2019.

[10] Z. Wu, Z. Yang, K. Ding, and G. He, "Transfer mechanism analysis of injected voltage harmonic and its effect on current harmonic regulation in FOC PMSM," *IEEE Trans. Power Electron.*, vol. 37, no. 1, pp. 820–829, Jan. 2022.

[11] T. Li, X. Sun, G. Lei, Y. Guo, Z. Yang, and J. Zhu, "Finite-control-set model predictive control of permanent magnet synchronous motor drive systems—An overview," *IEEE/CAA J. Autom. Sinica*, vol. 9, no. 12, pp. 2087–2105, Dec. 2022.

[12] X. Sun, T. Li, M. Yao, G. Lei, Y. Guo, and J. Zhu, "Improved finite-control-set model predictive control with virtual vectors for PMSHM drives," *IEEE Trans. Energy Convers.*, vol. 37, no. 3, pp. 1885–1894, Sep. 2022.

[13] M. Hu, H. Ahn, and K. You, "Speed tracking of SPMSM via super-twisting logarithmic fast terminal sliding-mode control," *IEEE Access*, vol. 11, pp. 91904–91912, 2023.

[14] X. Sun, Y. Xiong, J. Yang, and X. Tian, "Torque ripple reduction for a 12/8 switched reluctance motor based on a novel sliding mode control strategy," *IEEE Trans. Transport. Electrific.*, vol. 9, no. 1, pp. 359–369, Mar. 2023.

[15] Z. Jin, X. Sun, G. Lei, Y. Guo, and J. Zhu, "Sliding mode direct torque control of SPMSMs based on a hybrid wolf optimization algorithm," *IEEE Trans. Ind. Electron.*, vol. 69, no. 5, pp. 4534–4544, May 2022.

[16] J. Xu, H. Fang, Z. Liang, B. Zhang, and H. Guo, "Sensorless fault-tolerant control via high-frequency signal injection for aerospace FTPMSM drives with phase open- and short-circuit faults," *IEEE Trans. Transport. Electrific.*, vol. 8, no. 3, pp. 3401–3410, Sep. 2022.

[17] X. Sun, X. Tang, X. Tian, J. Wu, and J. Zhu, "Position sensorless control of switched reluctance motor drives based on a new sliding mode observer using Fourier flux linkage model," *IEEE Trans. Energy Convers.*, vol. 37, no. 2, pp. 978–988, Jun. 2022.

[18] J. Chen, X. Yuan, F. Blaabjerg, and C. H. T. Lee, "Overview of fundamental frequency sensorless algorithms for AC motors: A unified perspective," *IEEE J. Emerg. Sel. Topics Power Electron.*, vol. 11, no. 1, pp. 915–931, Feb. 2023.

[19] X. Sun, Y. Zhu, Y. Cai, Z. Zhu, and Y. Xiong, "Speed sensorless control of switched reluctance motors in full-speed range based on inductance characteristics," *IEEE Trans. Transport. Electrific.*, vol. 10, no. 2, pp. 4018–4028, Jun. 2024, doi: 10.1109/TTE.2023.3306876.

[20] Y. Zuo, C. Lai, and K. L. V. Iyer, "A review of sliding mode observer based sensorless control methods for PMSM drive," *IEEE Trans. Power Electron.*, vol. 38, no. 9, pp. 11352–11367, Sep. 2023.

[21] Y. Zhang, Z. Yin, J. Liu, R. Zhang, and X. Sun, "IPMSM sensorless control using high-frequency voltage injection method with random switching frequency for audible noise improvement," *IEEE Trans. Ind. Electron.*, vol. 67, no. 7, pp. 6019–6030, Jul. 2020.

[22] Y. Zhang, C. Chen, Z. Liu, Q. Chen, J. Zhang, and G. Liu, "Pseudo-random signal injection for position sensorless control of five-phase IPMSM based on third harmonic space," *IEEE Access*, vol. 11, pp. 145031–145041, 2023.

[23] J. Xu, H. Fang, B. Zhang, and H. Guo, "High-frequency square-wave signal injection based sensorless fault tolerant control for aerospace FTPMSM system in fault condition," *IEEE Trans. Transport. Electrific.*, vol. 8, no. 4, pp. 4560–4568, Dec. 2022.

[24] X. Sun, Y. Zhang, X. Tian, J. Cao, and J. Zhu, "Speed sensorless control for IPMSMs using a modified MRAS with gray wolf optimization algorithm," *IEEE Trans. Transport. Electrific.*, vol. 8, no. 1, pp. 1326–1337, Mar. 2022.

[25] H. Ding, X. Zou, and J. Li, "Sensorless control strategy of permanent magnet synchronous motor based on fuzzy sliding mode observer," *IEEE Access*, vol. 10, pp. 36743–36752, 2022.

[26] X. Sun, F. Cai, Z. Yang, and X. Tian, "Finite position control of interior permanent magnet synchronous motors at low speed," *IEEE Trans. Power Electron.*, vol. 37, no. 7, pp. 7729–7738, Jul. 2022.

[27] Q. Lu, Y. Wang, L. Mo, and T. Zhang, "Pulsating high frequency voltage injection strategy for sensorless permanent magnet synchronous motor drives," *IEEE Trans. Appl. Supercond.*, vol. 31, no. 8, pp. 1–4, Nov. 2021.

[28] X. Guo, S. Zeng, M. Wu, R. Zhong, and W. Hua, "A low-speed position sensorless scheme from standstill for low-cost SRM drives based on triple current slope difference threshold," *IEEE Trans. Ind. Electron.*, vol. 71, no. 4, pp. 3296–3306, Apr. 2024.

[29] S. Chen, W. Ding, X. Wu, R. Hu, and S. Shi, "Finite position set-phase-locked loop with low computational burden for sensorless control of PMSM drives," *IEEE Trans. Ind. Electron.*, vol. 70, no. 9, pp. 9672–9676, Sep. 2023.

[30] O. Lipcak and J. Bauer, "MRAS-based induction machine magnetizing inductance estimator with included effect of iron losses and load," *IEEE Access*, vol. 9, pp. 166234–166248, 2021.
[31] S. Ye and X. Yao, "An enhanced SMO-based permanent-magnet synchronous machine sensorless drive scheme with current measurement error compensation," *IEEE J. Emerg. Sel. Topics Power Electron.*, vol. 9, no. 4, pp. 4407–4419, Aug. 2021.
[32] C. Du, Z. Yin, J. Liu, Y. Zhang, and X. Sun, "A speed estimation method for induction motors based on active disturbance rejection observer," *IEEE Trans. Power Electron.*, vol. 35, no. 8, pp. 8429–8442, Aug. 2020.
[33] C. Gong, Y. Hu, J. Gao, Y. Wang, and L. Yan, "An improved delay-suppressed sliding-mode observer for sensorless vector-controlled PMSM," *IEEE Trans. Ind. Electron.*, vol. 67, no. 7, pp. 5913–5923, Jul. 2020.
[34] S. Morimoto, K. Kawamoto, M. Sanada, and Y. Takeda, "Sensorless control strategy for salient-pole PMSM based on extended EMF in rotating reference frame," *IEEE Trans. Ind. Appl.*, vol. 38, no. 4, pp. 1054–1061, Jul. 2002.
[35] J. Xu, Y. Du, B. Zhang, H. Fang, H. Guo, and Y.-H. Chen, "Sensorless fault-tolerant control with phase delay compensation for aerospace FTPMSM drives with phase open-circuit and short-circuit faults," *IEEE Trans. Ind. Electron.*, vol. 68, no. 6, pp. 4576–4585, Jun. 2021.
[36] C. M. Verrelli, S. Bifaretti, E. Carfagna, A. Lidozzi, L. Solero, F. Crescimbini, and M. Di Benedetto, "Speed sensor fault tolerant PMSM machines: From position-sensorless to sensorless control," *IEEE Trans. Ind. Appl.*, vol. 55, no. 4, pp. 3946–3954, Jul. 2019.
[37] J. Yang, W.-H. Chen, S. Li, L. Guo, and Y. Yan, "Disturbance/uncertainty estimation and attenuation techniques in PMSM Drives—A survey," *IEEE Trans. Ind. Electron.*, vol. 64, no. 4, pp. 3273–3285, Apr. 2017.
[38] M. Abdelrahem, C. M. Hackl, and R. Kennel, "Finite position set-phase locked loop for sensorless control of direct-driven permanent-magnet synchronous generators," *IEEE Trans. Power Electron.*, vol. 33, no. 4, pp. 3097–3105, Apr. 2018.
[39] R. Dian, J. Zhang, and Y. Jiang, "Improved MOGIFO-based flux observation strategy for PMSM sensorless drives," *IEEE Access*, vol. 12, pp. 28475–28483, 2024.
[40] X. Sun, T. Li, Z. Zhu, G. Lei, Y. Guo, and J. Zhu, "Speed sensorless model predictive current control based on finite position set for PMSHM drives," *IEEE Trans. Transport. Electrific.*, vol. 7, no. 4, pp. 2743–2752, Dec. 2021.
[41] X. Sun, J. Cao, G. Lei, Y. Guo, and J. Zhu, "Speed sensorless control for permanent magnet synchronous motors based on finite position set," *IEEE Trans. Ind. Electron.*, vol. 67, no. 7, pp. 6089–6100, Jul. 2020.
[42] A. K. W. Chee, "On the design principles of 3-D RESURF-enhanced RF SOI LDMOSFETs: Gate geometry optimization and rescaling," *IEEE Trans. Electron Devices*, vol. 69, no. 12, pp. 6523–6528, Dec. 2022.

CHEN ZHANG received the B.S. degree from Southeast University, Nanjing, China, in 2008, and the M.S. degree from Jiangsu University, Zhenjiang, China, in 2017.

He is currently an Experimenter with Huaiyin Institute of Technology. His research interests include magnetic bearings, bearingless motors, and nonlinear intelligent control of motors.

XIAO TANG is currently pursuing the bachelor's degree with Huaiyin Institute of Technology.

His research interests include magnetic bearings, bearingless motors, and nonlinear intelligent control of motors.

KUN XING received the B.S. degree from Huaiyin Institute of Technology, Huaian, China, in 2024.

He is currently a Senior Student with Huaiyin Institute of Technology. His research interests include magnetic bearings, bearingless motors, and nonlinear intelligent control of motor.

HENGRUI ZHOU received the B.S. degree from Huaiyin Institute of Technology, Huaian, China, in 2008, and the M.S. degree from Jiangsu University, Zhenjiang, China, in 2014.

He is currently an Experimenter with Huaiyin Institute of Technology. His research interests include automation control, the IoT, and power electronics technology.